Ocean Systems Engineering, *Vol. 14, No. 3 (2024) 277-299*
https://doi.org/10.12989/ose.2024.14.3.277

Experimental and numerical study on motion responses of modular floating structures with connectors in waves

Dong-Hee Choi, Jae-Min Jeon, Min-Ju Maeng, Jeong-Hyeon Kim and Bo Woo Nam*

Department of Naval Architecture and Ocean Engineering, Seoul National University,
Seoul 08826, Republic of Korea

(Received June 15, 2024, Revised August 25, 2024, Accepted September 13, 2024)

Abstract. In this study, the wave-induced motion responses of modular floating structures (MFS) was investigated through a series of experiments in a two-dimensional wave tank. A 1:63 scale model test was conducted using a 1-by-2 modular floating structure consisting of two modules and connectors. Two different types of connectors were considered: a pitch-free hinge and rigid connector. The numerical analysis was performed based on the higher-order boundary element method (HOBEM) and wave Green function with potential flow theory. First, the heave and pitch RAOs of the modules from the regular wave tests were directly compared with numerical analysis results. Next, the motion spectra and their statistical values from the irregular wave tests were compared with the numerical analysis results. The study revealed that the sheltering effect of the weather side module led to a reduction in motion of the lee side module. The numerical analysis showed good agreement with the experimental data, demonstrating the validity of the numerical method. Additionally, the rigid connector, which strongly constrain all six degrees of freedom, significantly reduce pitch motion, making the modules behave as a single rigid body.

Keywords: hinge connector; hydrodynamic analysis; model test; modular floating structures; numerical analysis; rigid connector

1. Introduction

Interest in ocean space utilization has been steadily increasing, particularly as coastal areas become more developed and space becomes limited. Traditionally, the primary method for expanding usable ocean space has been through land reclamation, which involves creating new land by filing in parts of the sea. This method has significant drawbacks, including severe environmental disruption and the requirement for substantial financial investment. In recent years, attention has shifted toward floating structures for ocean space utilization as a promising solution to these challenges. Unlike traditional land reclamation, these floating structure can be deployed with minimal environmental impact and at a potentially lower cost, offering a flexible and scalable approach to ocean space utilization.

Several real-world examples highlight the growing interest and viability of floating structures as a representative case of ocean space utilization. Japan's Mega-Float project, for instance, explored the use of a massive floating platform as a potential site for an offshore airport. (Isobe

---

*Corresponding author, Professor, E-mail: bwnam@snu.ac.kr

http://www.techno-press.org/?journal=ose&subpage=7 ISSN: 2093-6702 (Print), 2093-677X (Online)

1999) Similarly, the Floating Pavilion in the Netherlands demonstrates the potential for floating structures to support urban expansion (Storm 2016), while Singapore's Floating Solar Farm showcases the use of floating platforms for renewable energy production. (Zhang *et al.* 2024) These projects exemplify how floating structure can provide innovative solutions to the growing demand for ocean space, addressing both environmental and economic concerns. In more detail, according to Jiang *et al*. (2023), VLFS can be categorized into two main concepts: shape and functionality. In terms of shape, there are pontoon types and semi-submersible types. As for the functionality, VLFS can be categorized into transportation platforms, energy platforms and living platforms. In terms of transportation, a notable example is Japan's Mega-Float project (Isobe, 1997). For energy resources, studies have explored ocean wave energy converters including work by Crema (2018), Ikoma *et al*. (2019). In the area of wind turbines, relevant research includes studies by Zhang *et al*. (2021) and Li *et al*. (2022). Regarding living platforms, Wang and Tay (2011) have investigated residential areas, while Sevit Island, constructed for recreation and conference purposes was studies by Yun (2019).

In many cases, floating ocean space utilization platforms are designed using multiple modular units connected by various types of connectors. These connectors play a crucial role in restricting the six degrees of freedom (6-DOF) motions between adjacent floating modules. Connectors can be categorized based on the type of motion they primarily restrict. If a connector restricts all 6-DOF motions, it is classified as a rigid connector. Conversely, if it selectively restricts certain DOFs, it is generally referred to as a flexible connector. Rigid connectors have the advantage of strongly constraining the motion between modules, but they also bear the drawback of experiencing very high loads acting on the connectors. Notable proposed rigid connector designs include those by Bargeco (1985) and Song (2012). Flexible connectors, on the other hand, can be further divided into categories such as articulated, cable and vertical-free connection system. Articulated connectors, for instance, are designed to restrict rotational motion and have been proposed in various forms depending on the material or method used to physically implement the hinge-type connection. Early designs include Haney's (1999) model, which used horizontal pegs and docking probes to free only the pitch motion. Other designs include McAllister's (1997) use of rubber cones and spherical hinged heads and Zhu's (2015) proposal of the more advanced Flexible Base Hinged Connector (FBHC). In addition to articulated connectors, other designs include various forms of cable connectors proposed by Derstine and Brown (2000), Nagai *et al*. (2006) and Xu *et al*. (2014). Vertical-free connectors have also been studied, with notable research contributions from Koekoek (2010) and Jiang *et al*. (2021).

To ensure that a floating structure can effectively performs its functions, it is crucial to accurately evaluate the hydrodynamic performance of its submerged components. Previous studies that have applied potential theory to the analysis of VLFS include Riggs and Ertekin (1993), Wu *et al*. (2003) and Huang *et al*. (2021), and due to the nature of VLFS, which often consists of multiple adjacent floating bodies, studies such as Lee and Choi. (1998) which applied the concept of generalized mode for solving the radiation boundary condition have been conducted to consider the multi-body hydrodynamic interactions between these adjacent bodies. Also, to solve the boundary condition problem for potential solutions, methods such as the Constant Panel Method (CPM) and the High-Order Boundary Element Method (HOBEM) are employed. Liu *et al*. (1990) and Choi *et al*. (2001) demonstrated that HOBEM provides more accurate results and faster convergence when dealing with complex flow problems between adjacent floating bodies separated by gaps.

To accurately analyze the physical phenomena of complex floating systems, precise modeling must be complemented by model-scale experiments for validation. Recognizing the importance of model testing, many previous studies have conducted various experiments on different types of floating ocean space utilization system. These experiments range from relatively simple tests on modular structures connected by connectors between two modules to more complex setups involving a variety of module arrangements, connector combinations and diverse environmental conditions. Dong *et al.* (2024) investigated the motion and connector loads of a double-module floating structure connected with springs and fenders. Their study focused on understanding how different spring stiffness values affect the connector loads and platform motions. Shi *et al.* (2018) conducted model experiments on a three-module system restrained by complex spring devices, measuring hydro-elastic properties and comparing these with various numerical approaches for validation. Ding *et al.* (2020) performed model experiments on a three-module VLFS under shallow water and uneven seabed conditions, comparing the results with numerical analysis based on hydro-elasticity theory. Also, Wu *et al.* (2018) carried out model tests on a three-VLFS system deployed near islands and reefs. They also performed numerical simulations using Boussinesq equations and the Rankine source method. For more sophisticated module arrangements, Waals *et al*. (2018) and Otto *et al*. (2019, 2020) explored a total 87 triangular multi-island artificial structure connected by diverse springs and fenders. They conducted model tests and validated the results through frequency-domain numerical analysis based on potential theory.

In this study, a series of model test were performed to examine the motion responses of modular floating structures (MFS) in regular and irregular waves. Two types of connectors were selected for the test: a rigid connector and a hinge connector, with the latter being represented by a hinge that provides rotational freedom only in the pitch direction. Numerically, the analysis was performed in the frequency domain using potential flow theory, incorporating multibody interactions between two rectangular modules. High-Order Boundary Element Method (HOBEM) with wave Green function was employed for the numerical computation. The stiffness of the connectors was also linearized to suit the frequency domain analysis. Section 2 provide the details of the experimental setup, while Section 3 describes the numerical method. Section 4 contains the results and discussions, where direct comparisons between the experimental data and numerical analysis results are presented, and discussions are made on the motion characteristics of the MFS modules depending on the connector types.

2. Experimental setup

2.1 Experimental model

The primary objective of this experiment is to understand the motion characteristics of each module when two adjacent floating bodies are connected by specific types of connectors. The full-scale MFS module has a square shape with both its length and width of 60 m, and a height of 10 m. In the experiment, the scaled model was made of acrylic with a thickness of 8 mm to ensure rigid-body characteristics without deformation, and a 1:63 scale was applied, considering the width limit of the wave tank. Additionally, mass was appropriately distributed inside and outside the acrylic model to replicate the desired mass distribution of the full-scale version. Detailed specifications for both the full-scale and model-scale modules are provided in Table 1. The same model, based on these specifications, was used for both adjacent bodies. The gap between the two modules was set to 3.0 m at full scale, which corresponds to the width of the 2D wave tank minus

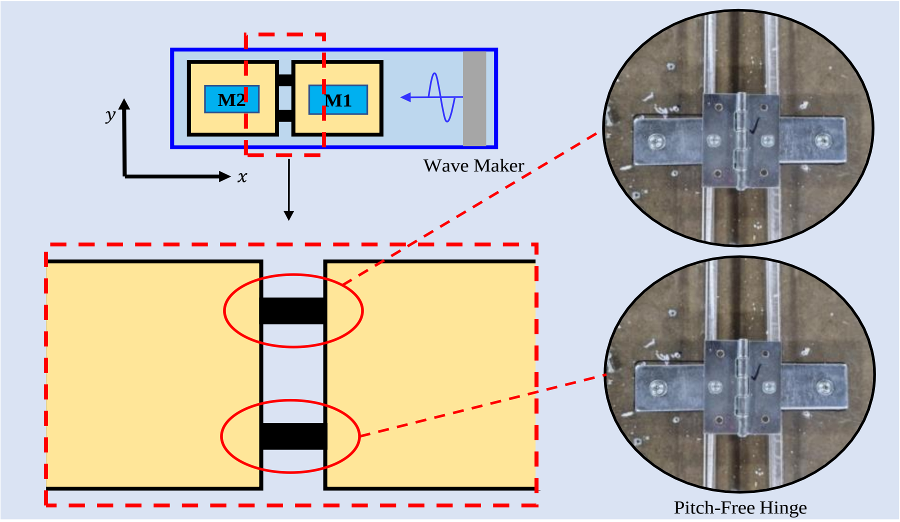

(a) Hinge connectors

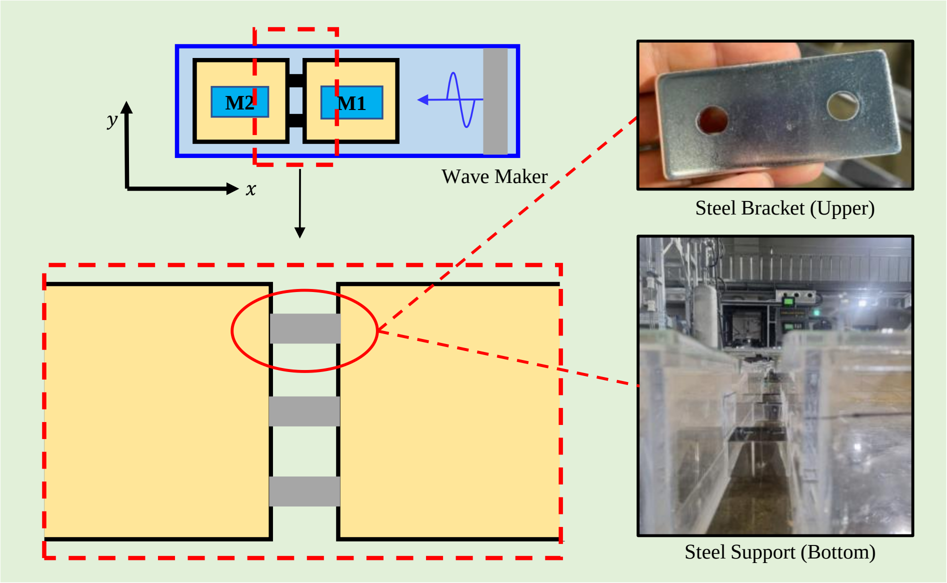

(b) Rigid connectors

Fig. 1 Arrangement diagrams of the pitch-free hinge (upper) and rigid connectors (lower)

width of the experimental model at the model scale. This arrangement facilitates the numerical analysis by allowing the floating body problem to be addressed in the presence of walls using the Method of Images (Newman 2018).

In this study, two types of connectors were applied between the modules: a hinge connector that allows a single rotational degree of freedom and a rigid connector that constrains all translational and rotational motions. The layout of these connectors is detailed in Fig. 1. For the hinge connector, as shown in Fig. 1(a), two pitch-free hinges were installed between the modules at

Table 1 Main particulars of the single module

Components	*Designation*	*Real Scale(1:1)*	*Model Scale(1:63)*
Single Module	Length	60 m	0.9524 m
	Height	10 m	0.1587 m
	Draft	7.875 m	0.1250 m
	Total Mass	$2.95058 \times 10^7\ kg$	116.21 kg
	Radius of Gyration(k_{xx})	19.19 m	0.3046 m
	Radius of Gyration(k_{yy})	19.19 m	0.3046 m
	Radius of Gyration(k_{zz})	22.01 m	0.3493 m

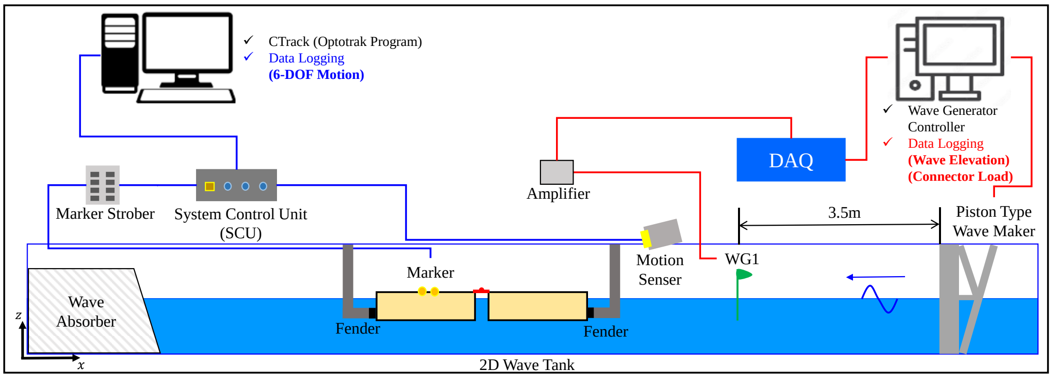

Fig. 2 The model test experimental arrangement layout diagram

equal intervals, allowing only pitch motion while constraining the other rotations in the roll and yaw directions. Similarly, for the rigid connectors, as depicted in Fig. 1(b). three steel brackets were installed on top of the modules at equal intervals, and a steel support was also attached at the bottom of the model to prevent bending.

2.2 Model test arrangement

The model test was conducted in the 2D wave tank at Seoul National University. The 2D wave tank has dimensions of 20.0 m (length)×1.0 m (width)×1.2 m (depth) and is equipped with a piston-type wave generator. A schematic layout of the experimental model arrangement and measurement system in the 2D wave tank is shown in Fig. 2. In this setup, module M1 is designated as the weather-side module, while module M2 represents the leeward-side module. Additionally, to prevent drift motion of the modules in the surge direction, fenders were installed at the fore and aft of the modular floating structure. The water depth was set to 0.5 m in the model scale, corresponding to a full-scale depth of 31.5 m.

The motion of the MFS modules was measured using the 6-DOF high-precision optical tracking system. This system tracks the 3D positions of markers attached to the models to determine the rigid body motion in real-time. The accuracy of motion measurement is about 0.1 mm for translations and 0.1 degrees for rotations. The sampling frequency was 20 Hz. The markers are placed on the deck center of the module, as depicted in Fig. 2 as yellow circular symbols. All measured motion values were converted into the motion data at the center of gravity of each module.

2.3 Wave condition

To assess the motion responses of the MFS modules under various wave conditions, model tests were conducted under 23 regular wave conditions, with periods ranging from 4.7 s to 31.8 s at full scale, as well as under three irregular wave conditions. The wave height for the regular wave conditions corresponds to H = 1.89 m at full scale. For the irregular waves, the JONSWAP wave spectrum with $\gamma = 3.3$ was used, and the significant wave height value was set to $H_s = 2\ m$ at full scale. The peak periods for the irregular waves are $T_p = 10.0, 11.0,$ and 12.0 s. The detailed specifications of the experimental wave conditions are presented in Tables 2 and 3 below.

3. Numerical method

3.1 High order boundary element method

The hydrodynamic analysis for the MFS system was performed based on potential flow theory, assuming inviscid, incompressible fluid and irrotational flow. In this study, the Higher-Oder Boundary Element Method (HOBEM) is applied to solve the linear boundary value problem, utilizing 9-node biquadratic elements for discretizing the floating body surface. The HOBEM is known for delivering more accurate solutions with faster convergence compared to constant panel methods, making it particularly effective for analysis involving closely spaced multiple floating free-surface and radiation boundary conditions, leading to the boundary integral equation presented in Eq. (1) with $\overrightarrow{r_0}$ denoting the positions of the source point distributed on the panel.

Table 2 Experimental conditions for the regular wave test (in real scale)

Wave ID	*Wave Direction*	*Wave Height*	*Periods*
RW#01~19	180°	1.89 m	$4.7\ s{\sim}11.9$ s with 0.4 s interval
RW#20	180°	1.89 m	13.89 s
RW#21	180°	1.89 m	15.87 s
RW#22	180°	1.89 m	23.81 s
RW#23	180°	1.89 m	31.74 s

Table 3 Experimental conditions for the irregular waves (in real scale)

Wave ID	*Wave Direction*	*Significant Wave Height(H_s)*	*Peak Periods(T_p)*
IRW#01	180°	2.0 m	10.0 s
IRW#02	180°	2.0 m	11.0 s
IRW#03	180°	2.0 m	12.0 s

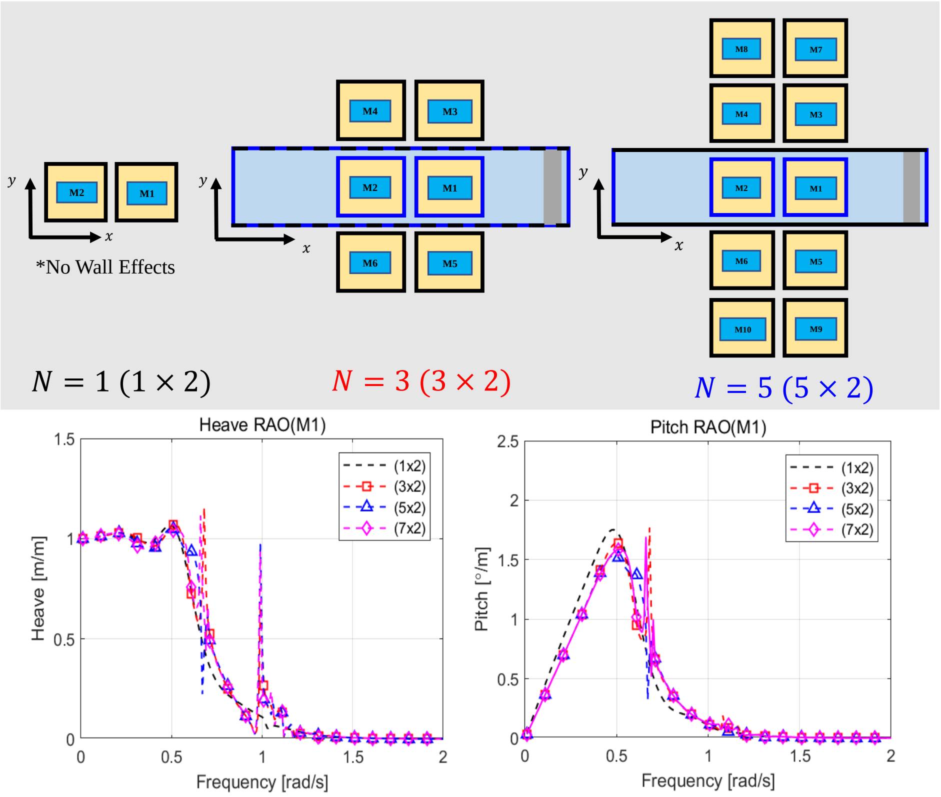

Fig. 3 Method of Images for the MFS model test in 2D wave tank

$$\phi(\vec{r_0})\left[1 + \nu \iint_{S_B} (\vec{r},\vec{r_0})dS\right] + \iint_{S_B}[\phi(\vec{r}) - \phi(\vec{r_0})]G(\vec{r},\vec{r_0})dS = \iint_{S_B} \phi(\mathrm{r})G(\vec{r},\vec{r_0})dS \tag{1}$$

By solving the boundary value problem, the linear velocity potential in the fluid domain with the presence of a floating body can be derived. Furthermore, this study extends the consideration of 6-DOF motion modes from a single rigid body to a multi-body system with $6 \times N$ generalized modes. N denotes the number of floating bodies. This extension allows for the consideration of flow and the motion of floating bodies in close proximity, incorporating a radiation boundary condition for the multi-body system. (Lee and Choi 1998)

Since the model test was conducted in the 2D wave tank, the boundary conditions for the walls on both sides of the MFS body had to be considered. In this study, the Method of Images was employed to address the boundary conditions imposed by the walls in the 2D wave tank. The Method of Images is particularly useful for dealing with boundary conditions in the presence of solid surfaces by replacing the effect of a solid boundary on fluid flow with an equivalent distribution of image bodies at locations that the boundary conditions are satisfied. Fig. 3 illustrates the process of placing image floating bodies on either side of the floating body of interest in the 2D wave tank. In this study, the image bodies were arranged at intervals equal to the gap distance between modules M1 and M2. In principle, as the number of image floating bodies increases, the boundary conditions at the walls are more accurately reflected, as shown in Fig. 3. Through a series of convergence tests, a 5 by 2 module arrangement was applied for the present

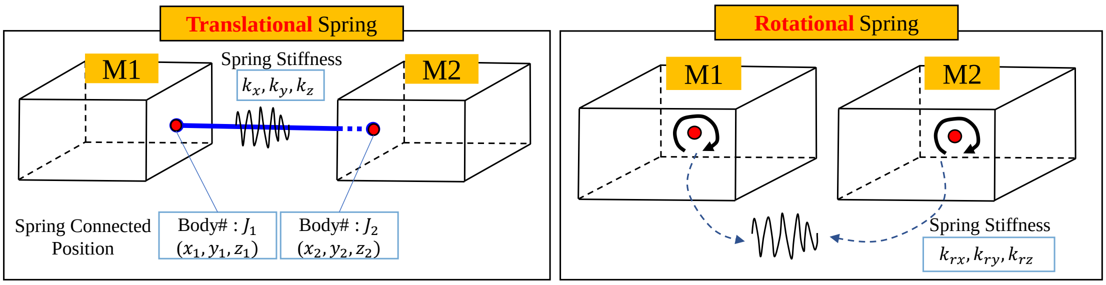

Fig. 4 Descriptions of the translational and rotational springs

numerical analysis, where the analysis accuracy converged to within approximately 6% in terms of motion RAO values.

3.2 Stiffness matrix due to connectors

To implement the stiffness effects introduced by the connector between multiple floating bodies in the frequency domain motion analysis, it is necessary to linearize the constraints imposed by the connector on the motion between the two floating bodies using a stiffness matrix. (Nam and Hong 2021) Especially, to account for the effects of hinge and rigid connectors that constrain both the translational and rotational directions between two floating bodies, it is necessary to combine two types of constraint matrices, translational and rotational stiffness matrices. Fig. 4 shows the schematics of constraining the two modules using springs in both translational and rotational directions.

Firstly, to achieve the translational motion constraints, this study adopted a simple linear spring. The stiffness effect of the linear spring can be implemented using the matrices provided in Eqs. (2)-(5).

$$[\boldsymbol{K}^e]_{3\times6} = \begin{bmatrix} -k_x & 0 & 0 & k_x & 0 & 0 \\ 0 & -k_y & 0 & 0 & k_y & 0 \\ 0 & 0 & -k_z & 0 & 0 & k_z \end{bmatrix} \tag{2}$$

$$[\boldsymbol{T}^e]_{6\times12} = \begin{bmatrix} 1 & 0 & 0 & 0 & z_1 & -y_1 & 0 & 0 & 0 & 0 & 0 & 0 \\ 0 & 1 & 0 & -z_1 & 0 & x_1 & 0 & 0 & 0 & 0 & 0 & 0 \\ 0 & 0 & 1 & y_1 & -x_1 & 0 & 0 & 0 & 0 & 0 & 0 & 0 \\ 0 & 0 & 0 & 0 & 0 & 0 & 1 & 0 & 0 & 0 & z_2 & -y_2 \\ 0 & 0 & 0 & 0 & 0 & 0 & 0 & 1 & 0 & -z_2 & 0 & x_2 \\ 0 & 0 & 0 & 0 & 0 & 0 & 0 & 0 & 1 & y_2 & -x_2 & 0 \end{bmatrix} \tag{3}$$

$$[\boldsymbol{R}^e]_{3\times3} = \begin{bmatrix} 0 & -z_1 & y_1 \\ z_1 & 0 & -x_1 \\ -y_1 & x_1 & 0 \end{bmatrix} \tag{4}$$

$$[\mathbf{K}^{Trans}]_{12\times12} = \begin{bmatrix} [\boldsymbol{K}^e]_{3\times6}[\boldsymbol{T}^e]_{6\times12} \\ [\boldsymbol{R}^e]_{3\times3}[\boldsymbol{K}^e]_{3\times6}[\boldsymbol{T}^e]_{6\times12} \\ -[\boldsymbol{K}^e]_{3\times6}[\boldsymbol{T}^e]_{6\times12} \\ -[\boldsymbol{R}^e]_{3\times3}[\boldsymbol{K}^e]_{3\times6}[\boldsymbol{T}^e]_{6\times12} \end{bmatrix} \tag{5}$$

Here, $[\boldsymbol{K}^e]_{3\times6}$ refers to the stiffness matrix where, the components k_x, k_y, k_z denotes the stiffness constants for the translational displacement between both bodies. Local position vectors (x_1, y_1, z_1) and (x_2, y_2, z_2) indicates the connection points of each M1 and M2 modules based on each module's global coordinates. And by applying the transformation matrix $[\boldsymbol{T}^e]_{6\times12}$ and rotation matrix $[\boldsymbol{R}^e]_{3\times3}$ to the motion response at global coordinates, the global restoring forces of each modules can be derived as below

$$\begin{bmatrix} F_{n+1} \\ F_{n+2} \\ F_{n+3} \end{bmatrix} = [\boldsymbol{K}^e]_{3\times6} \begin{bmatrix} s_{n+1} \\ s_{n+2} \\ s_{n+3} \\ s_{m+1} \\ s_{m+2} \\ s_{m+3} \end{bmatrix} = [\boldsymbol{K}^e]_{3\times6} [\boldsymbol{T}^e]_{6\times12} \begin{bmatrix} \xi_{n+1} \\ \xi_{n+2} \\ \xi_{n+3} \\ \xi_{n+4} \\ \xi_{n+5} \\ \xi_{n+6} \\ \xi_{m+1} \\ \xi_{m+2} \\ \xi_{m+3} \\ \xi_{m+4} \\ \xi_{m+5} \\ \xi_{m+6} \end{bmatrix} \tag{6}$$

$$\begin{bmatrix} F_{n+4} \\ F_{n+5} \\ F_{n+6} \end{bmatrix} = [\boldsymbol{K}^e]_{3\times6} \begin{bmatrix} s_{n+1} \\ s_{n+2} \\ s_{n+3} \\ s_{m+1} \\ s_{m+2} \\ s_{m+3} \end{bmatrix} = [\boldsymbol{R}^e]_{3\times3} [\boldsymbol{K}^e]_{3\times6} [\boldsymbol{T}^e]_{6\times12} \begin{bmatrix} \xi_{n+1} \\ \xi_{n+2} \\ \xi_{n+3} \\ \xi_{n+4} \\ \xi_{n+5} \\ \xi_{n+6} \\ \xi_{m+1} \\ \xi_{m+2} \\ \xi_{m+3} \\ \xi_{m+4} \\ \xi_{m+5} \\ \xi_{m+6} \end{bmatrix} \tag{7}$$

Here, ξ_n indicates the global motion response and F_n as global restoring force applied to the body M1. Also, $n = 6 \times (J_1 - 1)$ and $m = 6 \times (J_2 - 1)$ with $J_1 - th$ and $J_2 - th$ body. With above equations, if the two connection points of the spring are set to be identical and the values of the k_x, k_y, k_z are assigned extremely large values, approaching infinity, a translational stiffness matrix can be constructed that completely constrains the translational motion of the two floating bodies along the three axes, allowing only rotational movement about a single point.

Secondly, the rotational stiffness matrix can be suggested in Eq. (8). Again, the rotational motions between each bodies can be completely constrained by applying the infinity values of rotational stiffness constants at k_{rx}, k_{ry} or k_{rz}. For example, pitch free hinge connection can be achieved by applying infinite value on k_{rx} and k_{rz}. By adding the translational and rotational stiffness matrices, the connector conditions that constrain both translational and rotational motions can be expressed in Eq. (9).

$$[\mathbf{K}^{Rot}]_{12\times 12}=\left[\begin{array}{cccccccccccc}
0 & 0 & 0 & 0 & 0 & 0 & 0 & 0 & 0 & 0 & 0 & 0\\
0 & 0 & 0 & 0 & 0 & 0 & 0 & 0 & 0 & 0 & 0 & 0\\
0 & 0 & 0 & 0 & 0 & 0 & 0 & 0 & 0 & 0 & 0 & 0\\
0 & 0 & 0 & k_{rx} & 0 & 0 & 0 & 0 & 0 & -k_{rx} & 0 & 0\\
0 & 0 & 0 & 0 & k_{ry} & 0 & 0 & 0 & 0 & 0 & -k_{ry} & 0\\
0 & 0 & 0 & 0 & 0 & k_{rz} & 0 & 0 & 0 & 0 & 0 & -k_{rz}\\
0 & 0 & 0 & 0 & 0 & 0 & 0 & 0 & 0 & 0 & 0 & 0\\
0 & 0 & 0 & 0 & 0 & 0 & 0 & 0 & 0 & 0 & 0 & 0\\
0 & 0 & 0 & 0 & 0 & 0 & 0 & 0 & 0 & 0 & 0 & 0\\
0 & 0 & 0 & -k_{rx} & 0 & 0 & 0 & 0 & 0 & k_{rx} & 0 & 0\\
0 & 0 & 0 & 0 & -k_{ry} & 0 & 0 & 0 & 0 & 0 & k_{ry} & 0\\
0 & 0 & 0 & 0 & 0 & -k_{rz} & 0 & 0 & 0 & 0 & 0 & k_{rz}
\end{array}\right] \tag{8}$$

$$\begin{bmatrix} F^*_{n+1}\\ F^*_{n+2}\\ F^*_{n+3}\\ F^*_{n+4}\\ F^*_{n+5}\\ F^*_{n+6}\\ F^*_{m+1}\\ F^*_{m+2}\\ F^*_{m+3}\\ F^*_{m+4}\\ F^*_{m+5}\\ F^*_{m+6} \end{bmatrix} = \left([\mathbf{K}^{Trans}]_{12\times 12}+[\mathbf{K}^{Rot}]_{12\times 12}\right) \begin{bmatrix} \xi_{n+1}\\ \xi_{n+2}\\ \xi_{n+3}\\ \xi_{n+4}\\ \xi_{n+5}\\ \xi_{n+6}\\ \xi_{m+1}\\ \xi_{m+2}\\ \xi_{m+3}\\ \xi_{m+4}\\ \xi_{m+5}\\ \xi_{m+6} \end{bmatrix} \tag{9}$$

4. Results and discussion

4.1 MFS with hinge connectors in regular waves

In this section, the motion responses of the two rectangular modules connected by a pitch-free hinge are discussed in terms of motion RAOs in regular waves. Fig. 5 compares the heave motion RAOs of the weather-side module M1 and the lee-side module M2. The solid and dashed lines represent the HOBEM analysis results, while the symbols denote the experimental data. For frequencies greater than 0.5 rad/s, the heave motion of the M1 module is more pronounced than that of the M2 module. This is because the M1 module, positioned on the weather side and directly exposed to the incident waves, acts as a shield, thereby reducing the motion of the lee-side M2 module. Interestingly, for frequency less than 0.5 rad/s, the heave motion of the lee-side M2 module is greater than that of the M1 module. According to the numerical calculations, the heave resonant response of the M2 module occurs at around 0.35 rad/s. It is worth noting that while the numerical analysis results clearly show gap resonance occurring at a frequency of 1.0 rad/s, the experimental data does not capture this resonance effect. This implies that the pumping resonant effect between the two modules is overestimated in the potential-flow-based solutions, but in reality, due to viscous and nonlinear effects, the resonant effect is not as profound. Overall, Fig. 5

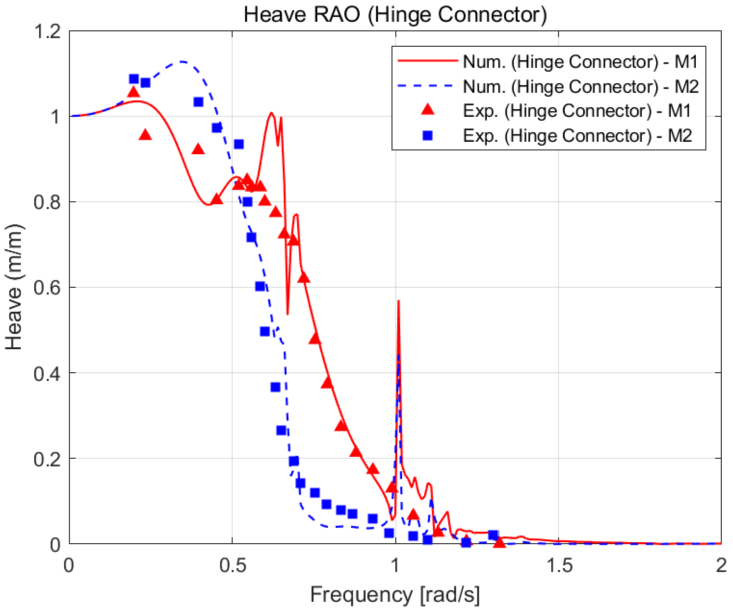

Fig. 5 Heave RAOs of the MFS modules with pitch-free hinge connectors

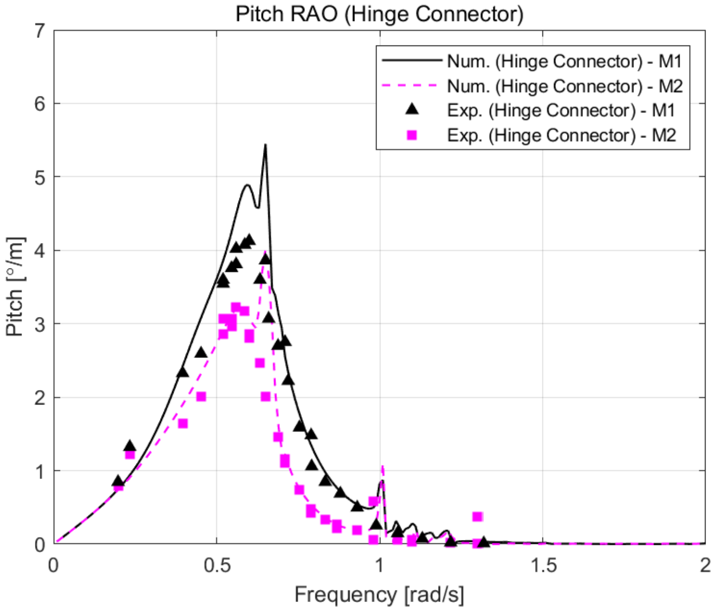

Fig. 6 Pitch RAOs of the MFS modules with pitch-free hinge connectors

demonstrates that the trend of heave motion in both M1 and M2 from the model test aligns well with the numerical results. The error between the model test data and the numerical analysis results was quantitatively expressed using the Root Mean Square Error (RMSE). The RMSE

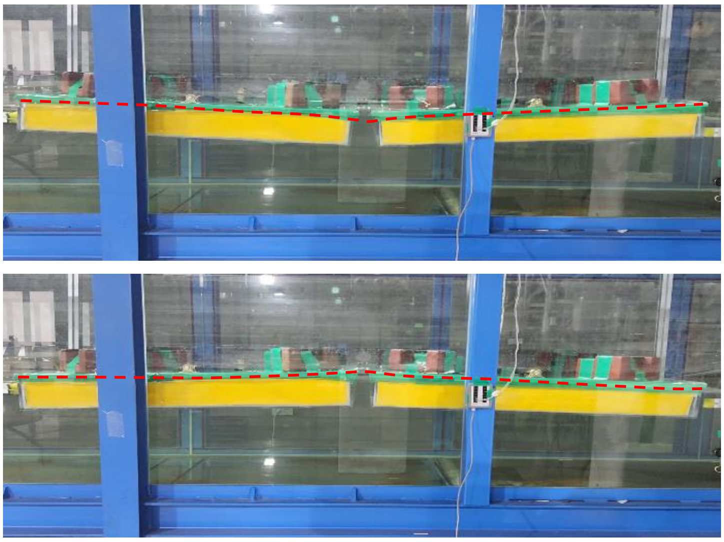

Fig. 7 Snapshots for the model test for the MFS with pitch-free hinge connectors in regular waves

between the two results indicated a difference of 8.44% for M1 and 6.87% for M2, demonstrating that the numerical results agree well with the model test outcomes. This comparison verifies the validity of the present numerical method.

Fig. 6 shows the RAO results of the pitch motions for both the M1 and M2 modules. The solid line represents the pitch RAO of the M1 module, and the dashed line represents the pitch RAO of the M2 module. The symbols indicate the model test data. Both the experimental data and numerical results confirmed that the M1 module on the weather side exhibited greater motion - about 50% higher in peak values - than the M2 module on the lee side due to the sheltering effect. Overall, the experimental data of M2 module closely matched the numerical analysis results. However, relatively large discrepancies can be observed between the numerical and experimental results, particularly near the peak RAO values of the weather side module. This can be attributed to the fact that vortex shedding and viscous effects were more pronounced, generating additional viscous damping due to the sharp-edged shape of the module. But, from a quantitative perspective, the RMSE between the two values was 7.77% for the M1 module and 4.00% for the M2 module, indicating small error margins. Fig. 7 shows snapshots of the MFS with pitch-free hinge connectors during the regular wave test at a wave frequency of 0.6 rad/s. As seen in the two images, the pitch motion of both modules occurred freely around the central connection point without any translational motion.

4.2 MFS with rigid connectors in regular waves

In this section, the motion responses of the MFS connected by rigid connectors in regular waves are discussed. Fig. 8 displays the heave RAO results of the two rectangular modules, where solid and dashed lines represent the numerical results, while the symbols denote the experimental data. When the wave frequency is less than 0.5 rad/s, the motion of the M1 module increases compared to the heave RAOs from the hinge connector case, while the motion of the M2 module slightly decreases. This can be explained by the fact that the rigid connector suppressed the

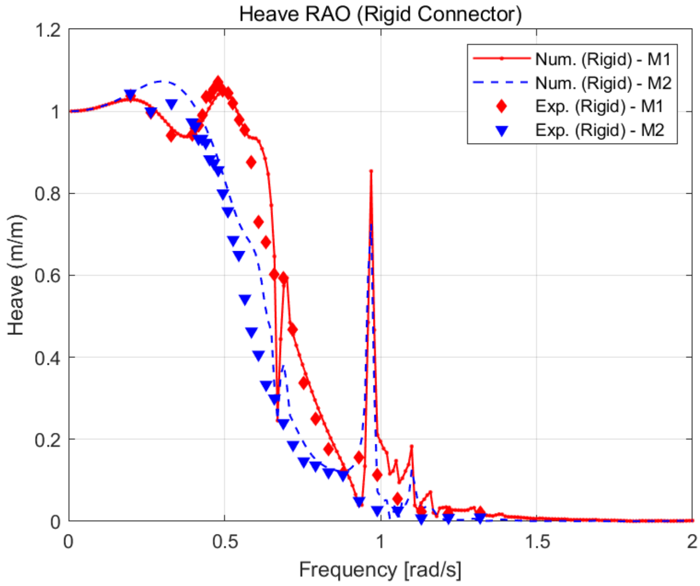

Fig. 8 Heave RAOs of the MFS modules with rigid connectors

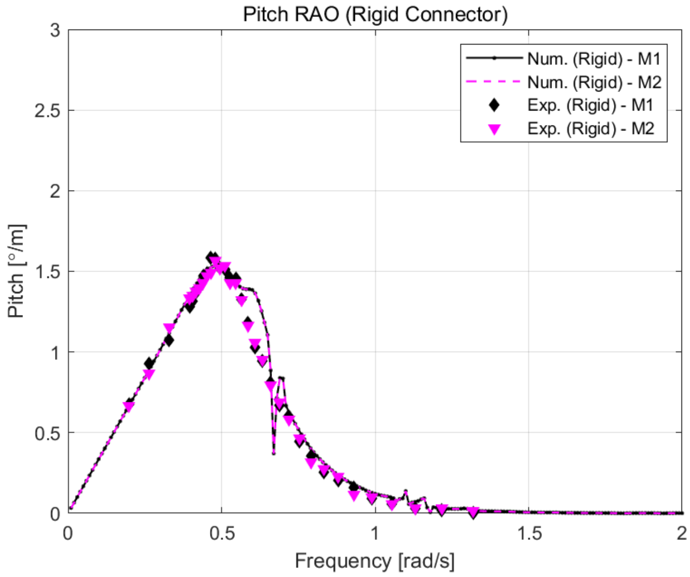

Fig. 9 Pitch RAOs of the MFS modules with rigid connectors

relative heave motion between the two modules, thereby reducing the motion differences. Similar to the hinge connector case, gap resonance can be observed at around 1.0 rad/s in the numerical analysis results due to the same gap distance, but it was not well captured in the experiments. For heave motion, the RMSE values were 6.66% for the M1 module and 9.30% for the M2 module, indicating good agreement between the experimental data and the numerical analysis results.

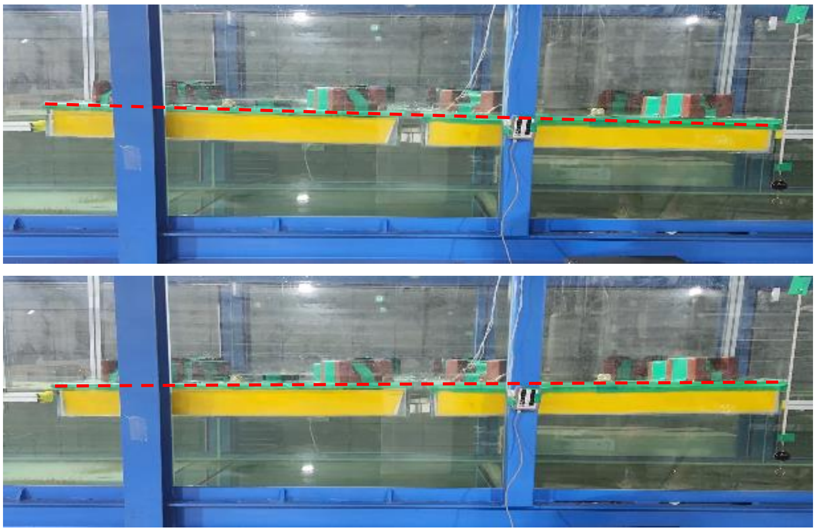

Fig. 10 Snapshots for the model test for the MFS with rigid connectors in regular waves

Fig. 9 shows the pitch RAOs of the module system constrained by a rigid connector. It can be observed that the RAO results for the pitch motion of the M1 and M2 modules were identical due to the strong constraint from the rigid connectors. This imply that the M1 and M2 modules move like a single rigid body with a large mass and inertia, rather than as two separate modules. This behavior of the MFS modules can be clearly seen in the snapshot at 0.5 rad/s shown in Fig. 10. Unlike the hinge configuration, the two modules do not move independently in the pitch direction; instead, they exhibit the same pitch angle, moving as if they were a single, large floating body. Due to the strong moment of inertia in the pitch direction, the pitch angle of motion is significantly smaller compared to other connector types. The peak pitch motion amplitude was reduced to 1.57 degrees, approximately 2.62 times lower than the maximum motion observed with the pitch free hinge. For the pitch RMSE values, 7.29% for the M1 module and 7.24% for the M2 module were observed, indicating a strong correlation between the model test and numerical analysis results.

4.3 MFS with hinge connectors in irregular waves

The motion response of MFS modules in irregular waves was investigated through the model test and directly compared with spectral analysis results based on motion RAOs from HOBEM calculations. Before conducting the model test in irregular wave conditions, wave calibration was performed on the wave elevations to be used in the experiment, ensuring they matched the target JONSWAP wave spectrum. Fig. 11 shows the wave calibration results for IRW #01~03 at full scale, confirming that the PSD values of the waves used in the model test closely match those used in the numerical analysis.

Fig. 12 shows the motion time series of the M1 module for the MFS with pitch-free connectors in irregular waves. First, the RMS values of heave motions were directly compared between the experimental data and the numerical analysis results, as shown in Fig. 13. It can be seen that the M1 module experiences notably higher heave motions than the M2 module, which aligns with the observations of the motion RAOs in Section 4.1. Additionally, the time series of the measured

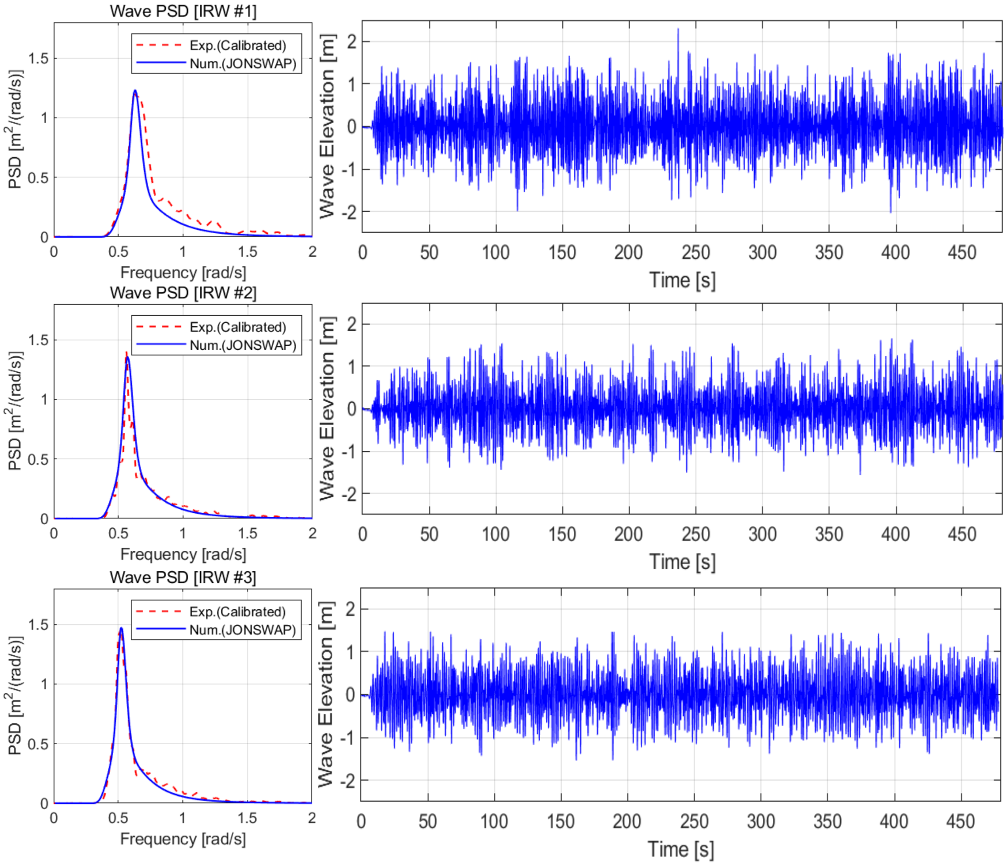

Fig. 11 Time series and PSD of the wave elevations for the irregular wave test (IRW#01~03)

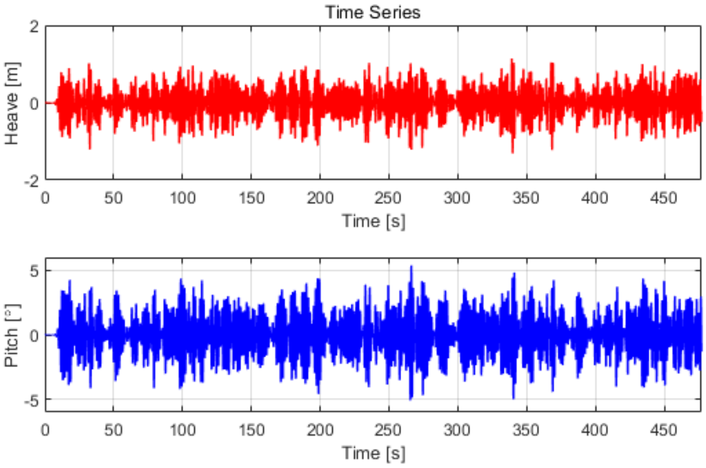

Fig. 12 Time series of the heave and pitch motions for the MFS module with hinge connectors in the irregular wave test (IRW#03)

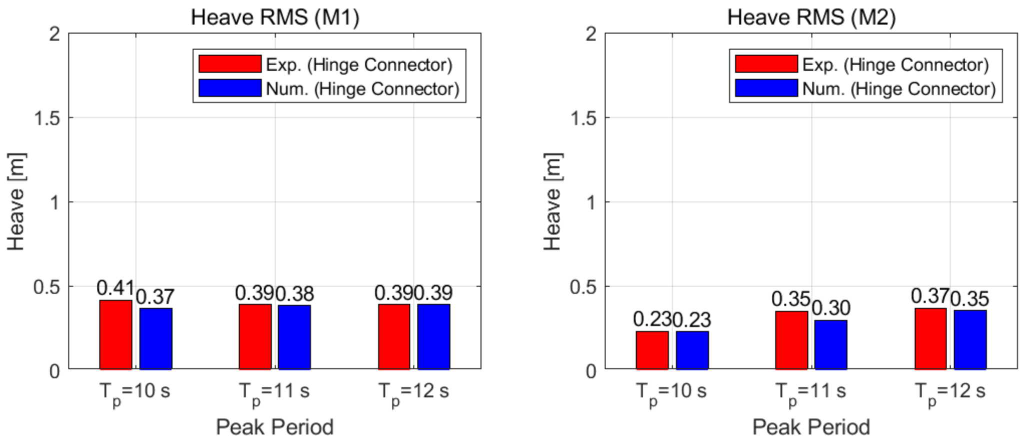

Fig. 13 Comparison of heave RMS values of the MFS modules with the hinge connectors in irregular waves

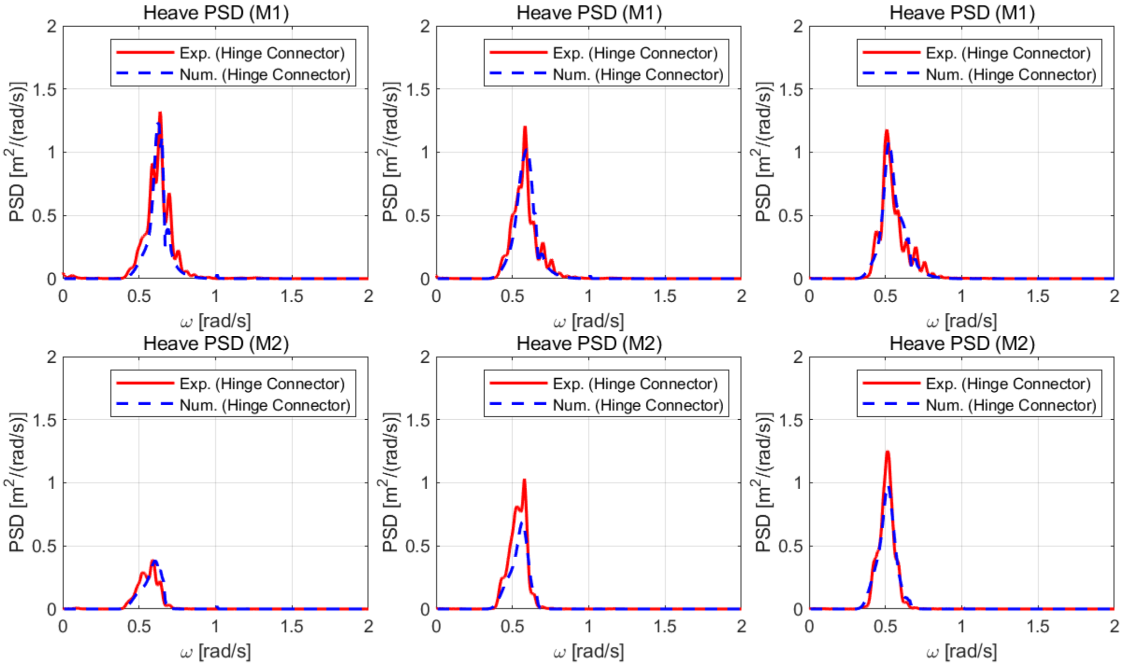

(a) (b) (c)

Fig. 14 Comparison of heave spectra of the MFS modules with the hinge connectors in irregular waves (a) Tp = 10.0 s, (b) Tp = 11.0 s and (c) Tp = 12.0 s

motions were transformed into power spectral density (PSD) plots using a fast Fourier transform. Fig. 14 shows the comparisons of the motion response spectra between the experiments and numerical calculations. Since the M2 heave RAO shows greater motion compared to the M1 module in frequency range less than 0.5rad/s, a significant increase in heave motion can be

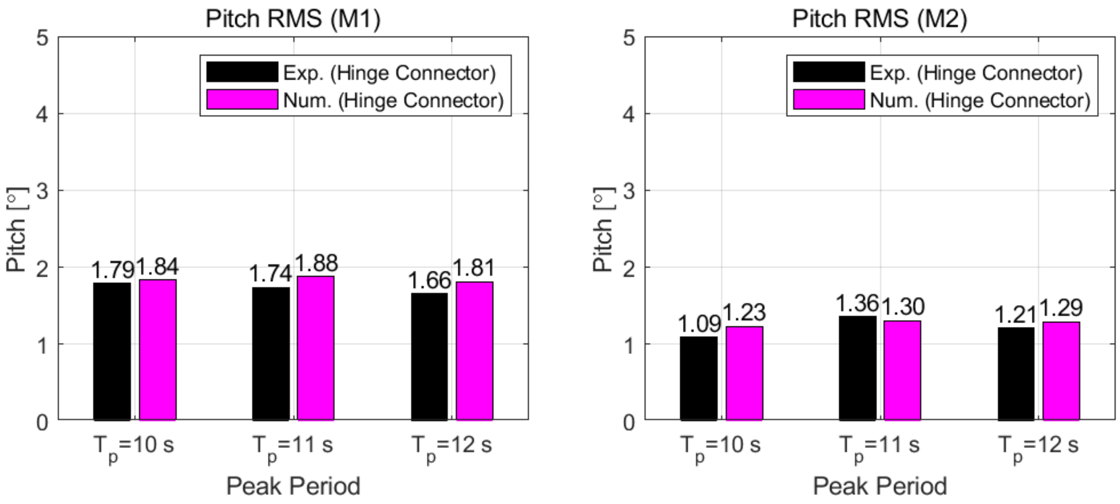

Fig. 15 Comparison of pitch RMS values of the MFS modules with the hinge connectors in irregular waves

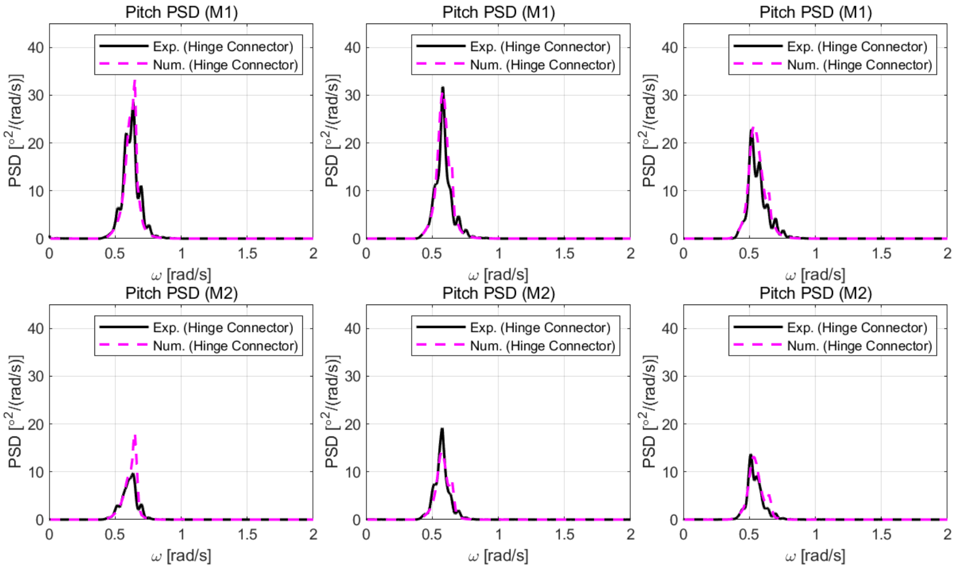

Fig. 16 Comparison of pitch spectra of the MFS modules with the hinge connectors in irregular waves (a) Tp = 10.0 s, (b) Tp = 11.0 s and (c) Tp = 12.0

observed in the heave RMS of the M2 in Fig. 13 and the heave spectra in Fig. 14 as T_p increases from 10 s to 12 s. This is because the wave peak frequency moves out of the sheltering-dominant frequency region and into the resonance region for M2's heave motion. A quantitative comparison of the errors between the experimental and numerical results was conducted by analyzing the RMS values for heave and pitch motions. For heave motion, the error values were 2.59% for the M1 module and 3.76% for the M2 module.

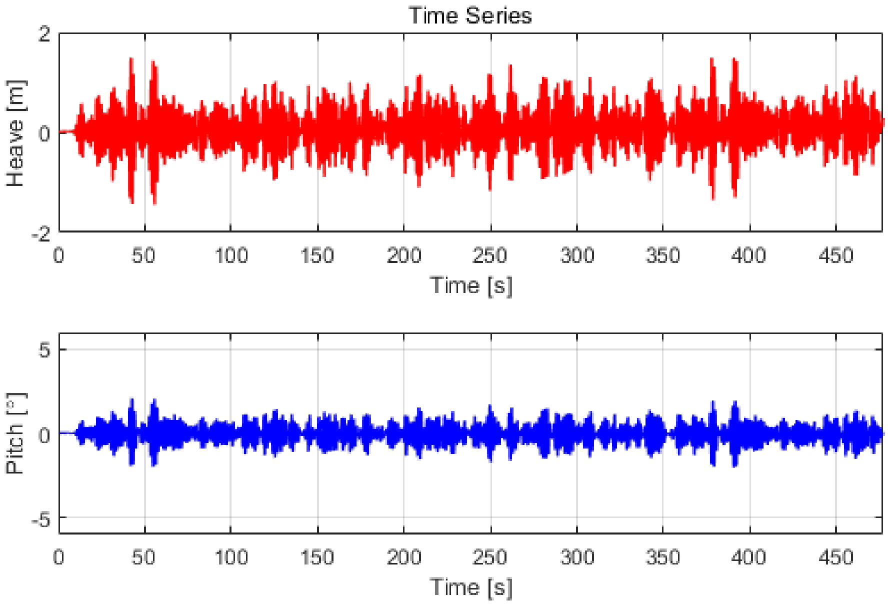

Fig. 17 Time series of the heave and pitch motions for the MFS module with the rigid connectors in the irregular wave test (IRW#03)

Fig. 15 compares the RMS values of pitch motions between the experimental data and the numerical analysis results. Since the motion RAOs of the M1 module are larger than those of the M2 module across all frequency ranges due to the effects of sheltering, as shown in Fig. 6, the RMS values for the M1 module are higher than those for the M2 module in all three irregular wave conditions. Both the experimental data and numerical results confirmed that the weather-side module experienced pitch motion responses approximately 30% to 50% greater than those of the lee-side module in irregular waves. The same trend is also clearly observed in the pitch spectrum comparisons as shown in Fig. 16. Since both modules exhibit resonance periods near 0.58rad/s, the maximum pitch motion responses can be found when the wave peak period (Tp) reaches 11 s. In the case of pitch motion, the RMSE values were 3.65% for the M1 module and 3.92% for the M2 module. These results indicate that the experimental and numerical analyses are in very close agreements.

4.4 MFS with rigid connectors in irregular waves

In this section, the motion response of the MFS with rigid connector is presented by comparing the results between the model test and numerical analysis. Fig. 17 shows the motion time series of the M1 module for the MFS with rigid connectors in irregular waves. Notably, the pitch motion results are significantly reduced compared to those with the hinge connectors. The RMS values of heave motions were directly compared between the experimental data and the numerical analysis results, as shown in Fig. 18. Similar to the pitch-free hinge connector, the M2 module's heave motion was smaller than that of the M1 module across all three wave conditions due to the sheltering effect. This trend can also be found through the comparison of the motion spectra for

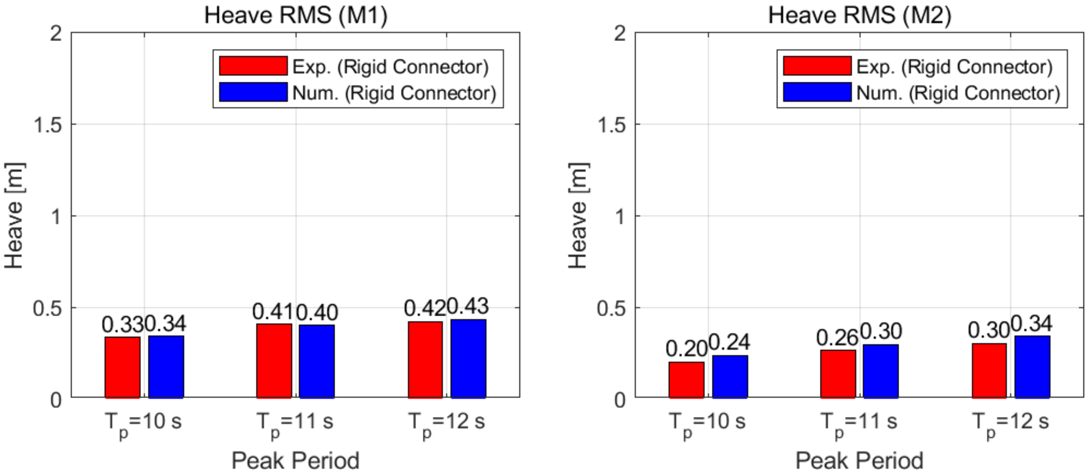

Fig. 18 Comparison of heave RMS values of the MFS modules with the rigid connectors in irregular waves

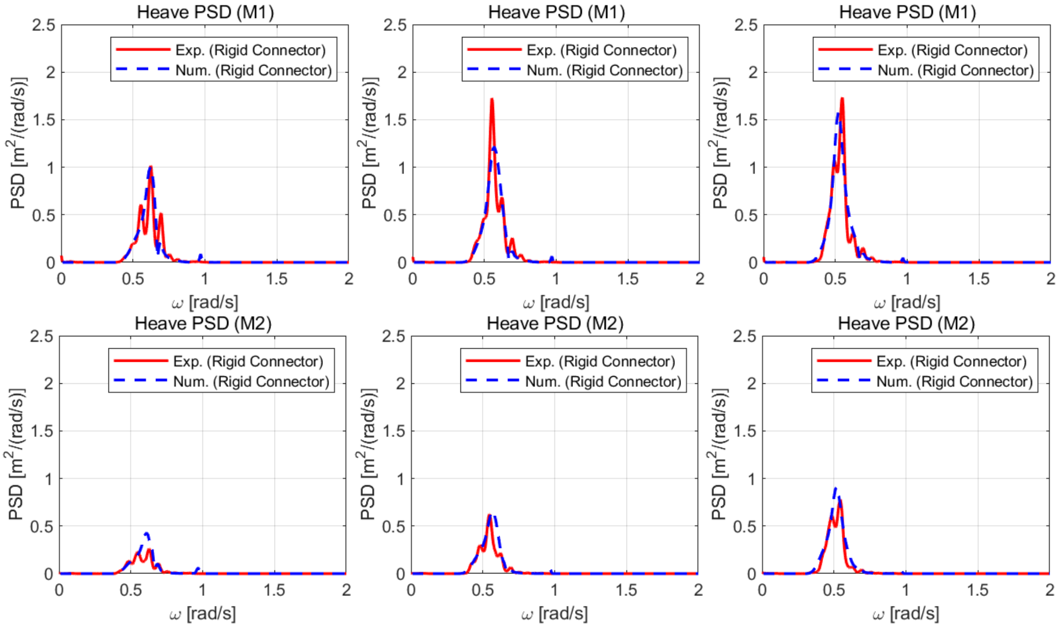

(a) (b) (c)

Fig. 19 Comparison of heave spectra of the MFS modules with the rigid connectors in irregular waves (a) Tp = 10.0 s, (b) Tp = 11.0 s, (c) Tp = 12.0 s

heave in Fig. 19. As seen in Fig. 19, the spectral response areas of M1 are significantly larger than those of M2, and the motion responses increases as the wave peak period increases. In the case of rigid connector, the heave RMSE values were 1.21% for the M1 module and 6.57% for the M2 module.

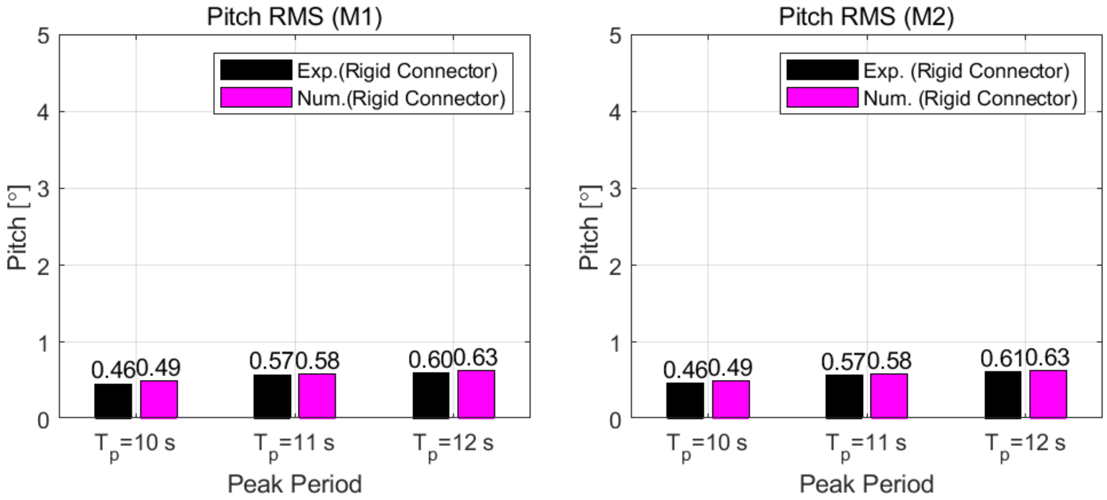

Fig. 20 Comparison of pitch RMS values of the MFS modules with the rigid connectors in irregular waves

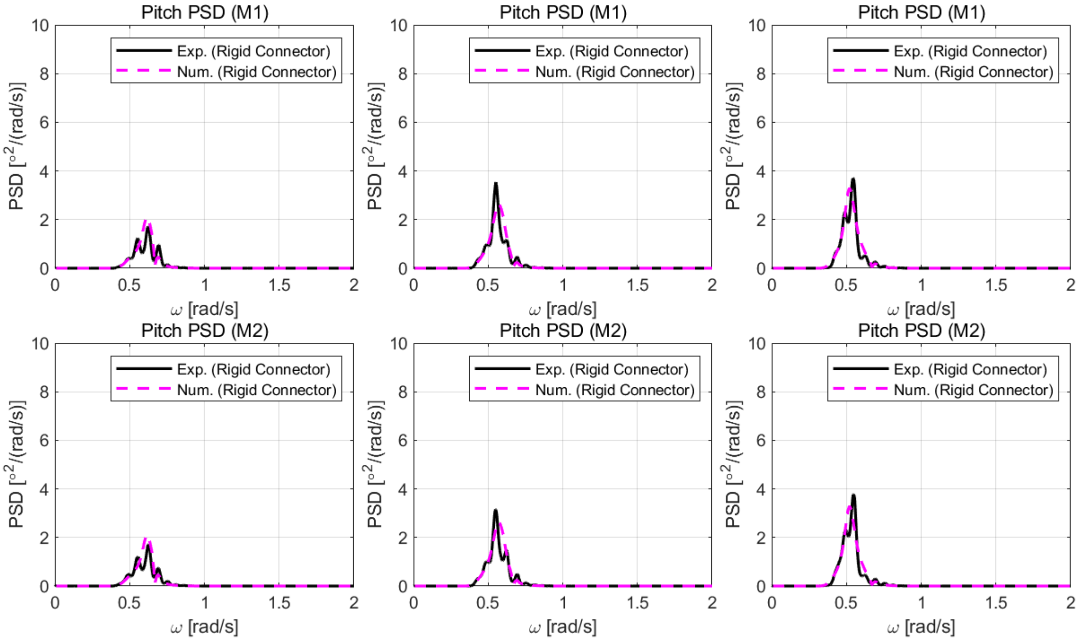

(a) (b (c)

Fig. 21 Comparison of pitch spectra of the MFS modules with the rigid connectors in irregular waves (a) Tp = 10.0 s, (b) Tp = 11.0 s and (c) Tp = 12.0 s

Fig. 20 shows the comparison between the RMS values of pitch motions of the experimental data and the numerical analysis results. Firstly, the pitch RMS values are less than 1° for all three wave conditions, which implies that the rigid connector strongly binds the two modules together, causing them to behave as a single large floating body. As a result, the pitch motion responses of both modules become the same. These pitch response of the MFS with rigid connector are significantly smaller than those of the MFS with hinge connectors. Fig. 21 presents the pitch spectra of the MFS modules with rigid connectors under three irregular wave conditions, which also shows that the pitch motion of both modules is identical and quite small. Overall, the RMS values of the motion responses slightly increase as the peak period increases. For pitch motion, the RMSE values were 2.34% for M1 and 1.93% for M2.

5. Conclusions

In this study, a series of model tests were conducted to examine the motion characteristics of the MFS modules in regular and irregular waves, depending on the type of connector used. Two rectangular modules were considered, with two types of connectors: hinge connectors and rigid connectors. The measured results were compared with the outcomes of frequency-domain numerical analysis based on the higher-order boundary element method with the wave Green function. The following conclusions were drawn from this study.

- When hinge connectors were applied, the motion responses of the lee-side module were significantly smaller than those of the weather-side module due to the sheltering effect. The results confirmed that the weather-side module exhibited pitch motion responses 30% to 50% greater than those of the lee-side module in irregular waves.
- When rigid connectors were applied, the two modules behave as a single large module, showing identical pitch motion responses. These pitch response of the MFS with rigid connector were significantly smaller than those of the MFS with hinge connectors.
- The numerical analysis showed good agreement with the experimental data, demonstrating the validity of the present HOBEM method based on potential flow theory combined with a linearized stiffness matrix for the connectors. However, the gap resonant effect is not as profound in the experiment due to viscous and nonlinear effects, while the numerical analysis results overestimated the pumping resonant effect between the two modules.

In the future research, focus should be placed on studies that measure the loads acting on the connectors. Additionally, three-dimensional model test will be performed, considering the various MFS arrangement of multiple modules.

Acknowledgements

This research was supported by the Korea Agency for Infrastructure Technology Advancement (KAIA) grant funded by the Ministry of Land, Infrastructure and Transport (Grant RS-2023-00250727) through the Korea Floating Infrastructure Research Center at Seoul National University.

References

Bargeco, A. (1985), “Securing of marine platforms in rough sea”, *Recent Pat. Eng.*, 104.

Choi, Y.R. and Hong, S.Y. (2002), "An analysis of hydrodynamic interaction of floating multi-body using higher-order boundary element method", *Proceedings of the 12th International Offshore and Polar Engineering Conference*, Kitakyushu, Japan.

Choi, Y.R., Hong, S.Y. and Choi, H.S. (2001), "An analysis of second-order wave forces on floating bodies by using a higher-order boundary element method", *Oceanic Eng.*, **28**(1), 117-138. https://doi.org/10.1016/S0029-8018(99)00064-5.

Crema, I. (2017), Oscillating water column wave energy converters integrated in very large floating structures.

Derstine, M.S. and Brown, R.T. (2000), "A compliant connector concept for the mobile offshore base", *Mar. Struct.*, **13**(4-5), 399-419. https://doi.org/10.1016/S0951-8339(00)00017-4.

Ding, J., Wu, Y.S., Zhou, Y., Ma, X.Z., Ling, H.J. and Xie, Z. (2020), "Investigation of connector loads of a 3-module VLFS using experimental and numerical methods", *Ocean Eng.*, **195**, 106684. https://doi.org/10.1016/j.oceaneng.2019.106684.

Dong, G., Mao, Y., Wu, Y., Ma, X., Yuan, F., Lu, X. and Zhang, L. (2024), "Experimental study on the hydrodynamic performance of a flexible connected double-module floating structure", *J. Offshore Mech. Arct. Eng.*, **146**(5). https://doi.org/10.1115/1.4064537.

Haney, J. (1999), "Mob connector development", *Proceedings of the 3rd International Workshop on Very Large Floating Structures*.

Huang, H., Chen, X.J., Liu, J.Y., Miao, Y.J. and Ji, S. (2021), "A method to estimate dynamic responses of VLFS based on multi-flating0module model connected by elastic hinges", *China Ocean Eng.*, **35**(5), 687-699. https://doi.org/10.1007/s13344-021-0061-9.

Ikoma, T., Masuda, K., Watanabe, Y., Eto, H., Theem, C.K. and Kinoshita, T. (2015), "Power generation potential of a VLFS equipped with OWC type WECs and damper effects on elastic motion", *Proceedings of the International Conference on Offshore Mechanics and Arctic Engineering*.

Isobe, E. (1999), "Research and development of Mega-Float", *Proceedings of the 3rd International Workshop on Very Large Floating Structures*.

Jiang, C., Xu, P., Bai, X., Zhao, Z., el Moctar, O. and Zhang, G. (2023), "A review of advances in modelling hydrodynamics and hydroelasticity for very large floating structures", *Ocean Eng.*, **285**, 115319. https://doi.org/10.1016/j.oceaneng.2023.115319.

Jiang, D., Tan, K.H., Wang, C.M. and Dai, J. (2021), "Research and development in connector systems for very large floating structures", *Ocean Eng.*, **232**, 109150. https://doi.org/10.1016/j.oceaneng.2021.109150.

Koekoek, M. (2010), Connecting modular floating structures: A general survey and structural design of a modular floating Pavilion (Master's thesis). TU Delft.

Lee, D.H. and Choi, H.S. (1998), "The motion behavior of shuttle tanker connected to a turret-moored FPSO", *Proceedings of the 3rd Int'l Conf on Hydrodynamics*.

Lee, D.H. and Choi, H.S. (1998), "The motion behavior of shuttle tanker connected to a turret-moored FPSO", *Proceedings of the 3rd Int'l Conference on Hydrodynamics*.

Li, Y., Ren, N., Li, X. and Ou, J. (2022), "Hydrodynamic analysis of a novel modular floating structure system integrated with floating artificial reefs and wave energy converters", *J. Mar. Sci. Eng.*, **10**(8), 1091. https://doi.org/10.3390/jmse10081091.

Liu, Y.H., Kim, C.H. and Lu, X.S. (1990), "Comparison of higher-order boundary element and constant panel methods for hydrodynamic loadings", *J. Offshore Polar Eng.*, **1**(1), 8-17.

McAllister, K.R. (1997), "Mobil offshore bases-an overview of recent research", *J. Mar. Sci. Technol.*, **2**, 173-181. https://doi.org/10.1007/BF02489808.

Nagai, B.M., Ameku, K., Nagai, Y. and Izumikawa, T. (2006), "Mooring method of very large floating structure", *Proceedings of the 16th International Offshore and Polar Engineering Conference*, OnePetro.

Nam, B.W. and Hong, S.Y. (2021), "Eigenvalue analysis for motion response of a TLP and tender semi considering a complex mooring configuration", *Int. J. Offshore Polar Eng.*, **31**(2), 169-177. https://doi.org/10.17736/ijope.2021.mm26.

Newman, J.N., 2018. Marine Hydrodynamics. The MIT Press.

Otto, W.J., Waals, O.J., Bunnik, T.H.J. and Ceneray, C. (2020), “Wave induced motions of a floating mega island”, *Proceedings of the WCFS2019 World Conference on Floating Solutions*.

Otto, W.J., Waals, O.J., Bunnik, T.H.J. and Cresp, J. (2019), “Optimization of wave induced motions and forces on a floating island”, *Proceedings of the ISOPE International Ocean Polar Engineering Conference*.

Riggs, H. and Ertekin, R. (1993), “Approximate methods for dynamic response of multi-module floating structures”, *Mar. Struct*., **6**(2-3), 117-141.

Shi, Q.J., Zhang, H.C., Xu, D.L., Qi, E.R., Tian, C., Ding, J., Wu, Y.S., Lu, Y. and Li, Z.W. (2018), “Experimental validation of network modelling method on a three-modular floating platform model”, *Coast. Eng*., **137**, 92-102. https://doi.org/10.1016/j.coastaleng.2018.04.001.

Song, B. (2012), “Research on the connector of very large floating offshore base”, *J. Ship Mech*.**,** **7**, 829-837.

Storm, W. (2016), Public Space in the Making: A Rotterdam Experiment. Streetnotes, 25.

Waals, O.J., Bunnik, T.H.J. and Otto, W.J. (2018), “Model tests and numerical analysis for a floating meta island”, *Proceedings of the 37th International Conference on Ocean*, Offshore & Arctic Engineering.

Wang, C.M. and Tay, Z.Y. (2011), “Very large floating structures: applications, research and development”, *Procedia Eng*., **14**, 62-72.

Wu, G., Shen, Q., Chen, X. and Wu, P. (2003), “Influence of the distance between floating bodies on hydrodynamic coefficients of floating multi-body system”, *Ocean Eng*., **21**(4), 29-34.

Wu, Y.S., Ding, J., Tian, C., Li, Z.W., Ling, H.J., Ma, X.Z. and Gao, J.L. (2018), “Numerical analysis and model tests of a three-module VLFS deployed near islands and reefs”, *J. Ocean Eng. Mar. Energ*., **4**, 111-122. https://doi.org/10.1007/s40722-018-0112-3.

Xu, D., Zhang, H., Qi, E., Hu, J. and Wu, Y. (2014), “On study of nonlinear network dynamics of flexibly connected multi-module very large floating structures”, In Vulnerability, Uncertainty and Risk: Quantification, Mitigation, and Management. American Society of Civil Engineers, 1805-1814.

Yun, J. (2019), “A copy is (not a simple) copy: Role of urban landmarks in branding Seoul as a global city”, *Front. Architect. Res*., **8**(1), 44-54. https://doi.org/10.1016/j.foar.2018.12.005.

Zhang, C., Dai, J., Ang, K.K. and Lim, H.V. (2024), “Development of compliant modular floating photovoltaic farm for coastal conditions”, *Renew. Sustain. Energ. Rev.*. **190**, 114084. https://doi.org/10.1016/j.rser.2023.114084.

Zhang, X., Lu, D., Liang, Y. and Brennan, F. (2021), “Feasibility of very large floating structure as offshore wind foundation: effects of hinge numbers on wave loads and induced responses”, *J. Waterw. Port, Coast. Ocean Eng*., **147**(3), 04021002. https://doi.org/10.1061/(ASCE)WW.1943-5460.0000626.

Zhu, X. (2015), Design and finite element analysis for very large floating structure flexible connector (Master’s thesis), Shanghai Jiaotong University.

MK